


# Deep-Learning-Enhanced Single-Spin Readout in Silicon Carbide at Room Temperature

Yu-Wei Liao,<sup>1,2</sup> Qiang Li,<sup>1,2,\*</sup> Mu Yang,<sup>1,2</sup> Zheng-Hao Liu<sup>①</sup>,<sup>1,2</sup> Fei-Fei Yan,<sup>1,2</sup> Jun-Feng Wang,<sup>1,2</sup> Ji-Yang Zhou,<sup>1,2</sup> Wu-Xi Lin,<sup>1,2</sup> Yi-Dan Tang<sup>①</sup>,<sup>3</sup> Jin-Shi Xu,<sup>1,2,†</sup> Chuan-Feng Li<sup>①</sup>,<sup>1,2,‡</sup> and Guang-Can Guo<sup>1,2</sup>

<sup>1</sup>*CAS Key Laboratory of Quantum Information, University of Science and Technology of China, Hefei 230026, People's Republic of China*

<sup>2</sup>*CAS Center For Excellence in Quantum Information and Quantum Physics, University of Science and Technology of China, Hefei 230026, People's Republic of China*

<sup>3</sup>*High-Frequency High-Voltage Devices and Integrated Circuits R&D Center, Institute of Microelectronics of Chinese Academy of Sciences, 100029, Beijing, China*

 (Received 21 April 2021; revised 13 August 2021; accepted 11 February 2022; published 16 March 2022)

Defect spin qubits in silicon carbide have recently drawn widespread attention. Extraction of spin information in the presence of noise always requires multiple repeated measurements, which consumes a large amount of time resources. In this paper, we propose a deep-learning-enhanced method to extract effective parameters from continuous-wave optically detected magnetic resonance (ODMR) spectra and Rabi oscillations with less time consumption. Even if the signal-to-noise ratio is reasonably low, a well-trained convolutional neural network (CNN) can predict the resonance peaks of ODMR spectra or the period of Rabi oscillations. Because of the fast output of predictions by the CNN, this method can be used to sense the magnetic field in the environment and microwave intensities in real time.

DOI: [10.1103/PhysRevApplied.17.034046](https://doi.org/10.1103/PhysRevApplied.17.034046)

## I. INTRODUCTION

Spin defects in silicon carbide (SiC) with near-infrared emission and a long spin coherence time have drawn much attention [1–13]. Compared with diamond, there are mature wafer-scale-fabrication and microprocessing and nanoprocessing techniques for SiC materials, and defect spin qubits can be integrated into chips with relatively low cost and high compatibility [14,15]. However, due to the finite photon count rate of a single spin defect, multiple repeated measurements are always necessary to obtain a high signal-to-noise ratio (SNR), even for spin defects with a relatively high spin-readout contrast. With fewer measurements, the SNR drops, and the spin signal may even become submerged in the noise, such as in the case of the optically detected magnetic resonance (ODMR) spectrum [16] and Rabi oscillations [17]. Fortunately, effective information derived from the spin signal still exists and can be extracted using a deep-learning method. Deep learning is part of a broader family of machine learning (ML) based on large amounts of data, named “big data.” Deep learning can allow us to catch sight of effective information

and a corresponding fitting function, and has been widely used in computer vision, speech recognition, and natural-language processing. Recently, ML methods have been widely used in quantum precision measurement, in quantum control and single-shot readout of nitrogen-vacancy (N-V) centers in diamond [18], in rapid classification of quantum photon sources [19], and in nuclear magnetic resonance [20]. ML-enhanced single-spin readout of N-V centers is achieved by combining Bayesian estimation and Hamiltonian learning to learn parameters in Ramsey sequences [21]. In this paper, we propose and demonstrate a deep-learning-enhanced method to extract spin signals directly from the ODMR spectrum or Rabi oscillations using well-trained deep neural networks.

The aim of the work presented here is to extract spin information from inferior raw data with a reasonably low SNR via a convolutional neural network (CNN) [22]. A brief introduction to CNNs is presented in Appendix A. Specifically, we experimentally generate a large number of ODMR spectra and Rabi oscillations with one-time and multitime measurement processes. We take the data from the one-time measurement process of the ODMR spectra or Rabi oscillations as features and label them by corresponding peak positions in the ODMR spectrum with 500-times measurement processes or by the frequency of the Rabi oscillations with 750-times measurement processes,

\*qianglee@ustc.edu.cn

†jsxu@ustc.edu.cn

‡cfli@ustc.edu.cn

respectively. After training with a substantial number of feature-label pairs, the CNN can predict an unknown ODMR spectrum's peak positions or the period of the Rabi oscillations with a low SNR. A well-trained CNN can be used for quantum sensing, since the peak positions in the ODMR spectrum and the Rabi-oscillation frequency are related to the ambient magnetic field intensity and the microwave (MW) power, respectively. Enhanced by deep learning, a real-time quantum sensing technology with a shorter time requirement and less resource consumption for measurements could be approached.

## II. EXPERIMENTAL SETUP

The structure of the CNN that we build is shown in Fig. 1. The input feature of the CNN is a one-dimensional vector of size  $1 \times 151$ , which is sampled from the normalized ODMR spectrum or Rabi oscillations. The CNN consists of three convolutional layers, and each layer is followed by a max-pooling layer, which is used to downsample the input vector into the feature space. The output of the convolutional path is flattened into a one-dimensional vector and sent to the fully connected path. There are two fully connected layers, with different numbers of neurons, in this path, which are used to fit the output values. When we input the ODMR spectrum, the size of the output layer is chosen as  $2 \times 1$ , corresponding to the two peak positions  $P_1$  and  $P_2$  in the ODMR spectrum. On the other hand, there is only one neuron in the output when we detect Rabi oscillations, which corresponds to the oscillation period ( $T$ ). Moreover, the activation functions of the CNN are chosen as the ReLu function [23], in order to increase the nonlinear fitting ability. The CNN is optimized by use of ADAM

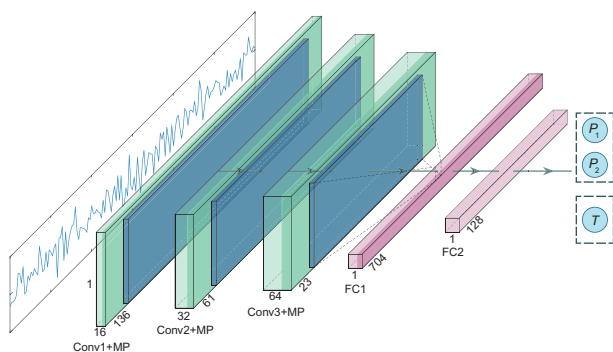


FIG. 1. Architecture of the convolutional neural network. The boxes represent the number and size of the feature maps extracted from the hidden layer. Conv,  $1 \times 4$  convolution layer with one stride; MP,  $1 \times 2$  max-pooling layer with two strides; FC, fully connected layer. There are two neurons,  $P_1$  and  $P_2$ , in the output layer when the peak positions of the ODMR spectrum are detected, and only one neuron,  $T$ , when the period of Rabi oscillations is detected.

[24] with a learning rate of  $10^{-6}$ , which can effectively prevent local optimization (see Appendix B for more details of the CNN).

Recently, we showed that single PL6 divacancy defects embedded in quantum wells in 4H-SiC had a high spin-readout contrast after integrating for a reasonably long time and had a high photon count rate [25,26]; the spin-readout contrast and photon count rate were comparable to those of N-V centers in diamond [27,28]. We focus on demonstrating the effect of the CNN on the spin readout based on such defects due to the convenience of obtaining the labels. However, this method can also be applied to enhance the spin readout of other spin defects.

A room-temperature home-built scanning confocal microscope combined with an ODMR measurement system is used to individually address and coherently control single spin qubits in the SiC. The experimental setup is specifically described in Appendix C. Figure 2(a) shows a representative confocal fluorescence image within an area

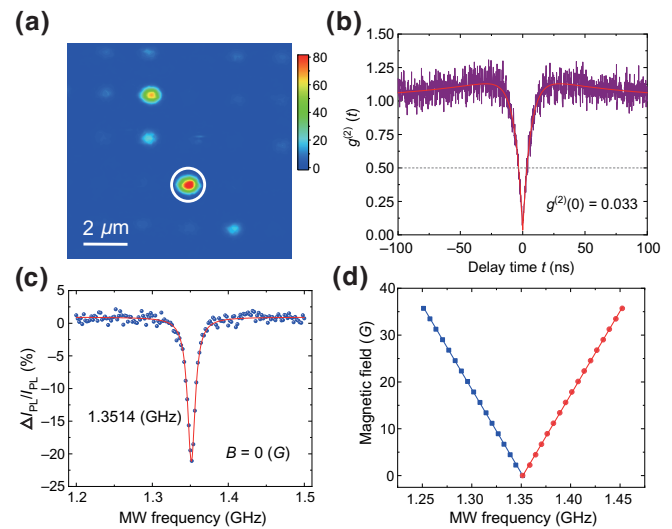


FIG. 2. Imaging and characterization of an isolated single defect. (a). Confocal fluorescence image ( $10 \times 10 \mu\text{m}^2$ ). The white scale bar is  $2 \mu\text{m}$ . The units of the color-scale bar are  $10^3$  counts/s. The bright point in the white circle is a single PL6 defect used in the present work. (b). Second-order intensity correlation function  $g^{(2)}(t)$  for an exciting laser power of 1 mW. The purple lines are the experimental data, and the red solid line is a corresponding fitting. At 0 delay time,  $g^{(2)}(0)$  is deduced to be 0.033, clearly indicating single-photon emission. (c). ODMR spectra of the single-defect spin in zero magnetic field. The experimental data (blue dots) are fitted with a Lorentz function (red solid line), from which the resonance frequency is deduced to be 1.3514 GHz. (d). Resonant frequency at different intensities of magnetic field (parallel to  $c$  axis). The red circles and blue squares are the resonance frequencies between  $m_s = 0$  and  $m_s = +1$  and between  $m_s = 0$  and  $m_s = -1$ , respectively. The red and blue solid lines are corresponding linear fittings. The inverse of the slope is deduced to be  $\pm 2.8$  MHz/G, respectively.

of  $10 \times 10 \mu\text{m}^2$  in the SiC sample, excited with a 1-mW laser. The bright point in the white circle is an isolated single PL6 defect used in the present work. Hanbury Brown and Twiss measurements [29] are performed to confirm the character of the single-photon emission. The second-order intensity correlation function  $g^{(2)}(t)$  for the fluorescence of the bright point excited with a 1-mW laser is shown in Fig. 2(b). The purple lines are the experimental results, and the solid red line is fitted by the function

$$g^{(2)}(t) = 1 - (1 + a)e^{-|t|/\tau_1} + de^{-|t|/\tau_2}, \quad (1)$$

where  $a$ ,  $d$ ,  $\tau_1$ , and  $\tau_2$  are fitting parameters [30–32]. From the fitting, the value of  $g^{(2)}(0)$  is deduced to be 0.033, clearly indicating that the bright point shown in Fig. 2(a) is a single-photon emitter.

The spin Hamiltonian of the neutral divacancy defects in 4H-SiC can be expressed as

$$H = \mu_B g \mathbf{B} \cdot \mathbf{S} + D[S_z^2 + S(S+1)/3] + E(S_x^2 - S_y^2), \quad (2)$$

where  $\mu_B$  is the Bohr magneton,  $g$  is the electron Landé  $g$ -factor ( $g = 2.0$ ),  $\mathbf{B}$  is the external magnetic field,  $\mathbf{S}$  ( $S = 1$ ) is the electron spin, and  $D$  and  $E$  are zero-field splitting parameters [33]. For the PL6 defect spins in 4H-SiC at room temperature,  $D = 1.351$  GHz [25,34]. Because of the spin-polarization-dependent emission, a change in the PL readout ( $\Delta I_{\text{PL}}$ ) with and without resonant MWs can be detected, which is the basis of continuous-wave (CW) ODMR measurements. For each point in a single one-time measurement process of the ODMR spectrum, the microwave signal is gated on and off with a 1-ms duration, and this is repeated ten times, such that the one-time measurement process consumes 3 s (see Appendix A for more detailed information). The measurement processes are repeated, and the scan results are averaged. The final ODMR spectra are calculated from  $\Delta I_{\text{PL}} = [\Sigma N(\text{on}) - \Sigma N(\text{off})]/\Sigma N(\text{off})$ , in which  $N(\text{on})$  and  $N(\text{off})$  are the photon counts with and without microwaves, respectively [35,36]. Figure 2(c) shows the CW ODMR spectra of a single defect spin in zero magnetic field, which are integrated by repeating the measurements 500 times. The blue dots are the raw experimental results, and the solid red line is the corresponding Lorentz fitting, from which the resonance frequencies between the spin ground state  $m_s = 0$  and  $m_s = \pm 1$  are 1.3514 GHz (the energy levels of the states  $m_s = \pm 1$  are degenerate in zero magnetic field). Figure 2(d) demonstrates the resonance frequency between the states  $m_s = 0$  and  $m_s = \pm 1$  in different intensities of the magnetic field (parallel to the  $c$  axis of the SiC). The blue squares (left branch) are the resonance frequency between  $m_s = 0$  and  $m_s = -1$ , while the red circles (right branch) are the resonance frequency between  $m_s = 0$  and  $m_s = +1$ . The solid red and blue lines are the corresponding linear fittings, from which the inverse of the slope is

deduced to be  $\pm 2.8$  MHz/G. These spin properties are consistent with previous work [1,25,34]. Through the above measurements, the spin qubits used in the present work are identified to be single electron spins of single PL6 defects in 4H-SiC.

### III. RESULTS

A representative ODMR spectrum from an individual one-time measurement process is shown in the upper panel of Fig. 3(a), where the ODMR signal is submerged in the noise. To label its peak, we take the ODMR spectrum obtained from a measurement process repeated 500 times as a standard. The standard peak positions are confirmed by Lorentz fitting, and the result is shown in the lower panel of Fig. 3(a). In order to train and test the CNN, 6200 inferior spectrum-peak pairs, which are detected for 16 different magnetic field intensities (12 for the training sets and 4 for the test sets), are generated and randomized into 6000 training sets and 200 test sets. We introduce the 1-norm as the loss function to quantify the training progress; this is defined as  $(1/2m) \sum_{i=1}^m \|\mathbf{y}_i - \mathbf{L}_i\|_1$ , where  $m$  is the number of samples;  $\mathbf{y}$  and  $\mathbf{L}$  are the output and label, respectively. With an increase in the epoch (a network-training period; see Appendix A for more information), the logarithm to base 10 of the 1-norm of the training (red) set and the test (blue) set drops swiftly and reaches about  $10^{-3}$  GHz when the epoch is more than 1500, as shown in Fig. 3(b). The results illustrate the CNN's capability to learn the spin signals from the inferior ODMR spectra and accurately predict their peak positions, which correspond to the resonance frequencies between different spin states. We further use the well-trained CNN to predict the ODMR peak positions for another single PL6 defect. The predicted precision is fully comparable to the results in Fig. 3(d) (see Appendix D for more details).

By combining the ODMR technique with the deep-learning method, we can achieve magnetic field sensing with fewer measurements and in less time. The intervals of the ODMR signal between the positions of the two peaks  $P_1$  and  $P_2$  are linear with the corresponding magnetic field intensities, which satisfy  $B = P_1 - P_2/2 \times 1/A$ , where  $A$  is a constant and its value in our experiment is 2.8 MHz/G according to Fig. 2(d), which is consistent with the electron gyromagnetic ratio for  $c$ -axis defect spins in 4H-SiC [33]. This property of defect spins in solid-state materials is often used for magnetic field sensing [34]. Here we compare the predicted magnetic field intensities  $B_{\text{pre}}$  (calculated from the predicted  $P_1$  and  $P_2$  in the test set) and the real magnetic field intensities  $B_{\text{real}}$  (calculated from  $P_1$  and  $P_2$  obtained from 500-times-repeated measurements of the ODMR spectrum), as shown in Fig. 3(c). The counts of  $(B_{\text{pre}}, B_{\text{real}})$  are gathered along the diagonal line  $B_{\text{pre}} = B_{\text{real}}$ .

In the case of fewer measurements, the deep-learning method shows a big advantage. Figure 3(d) presents a

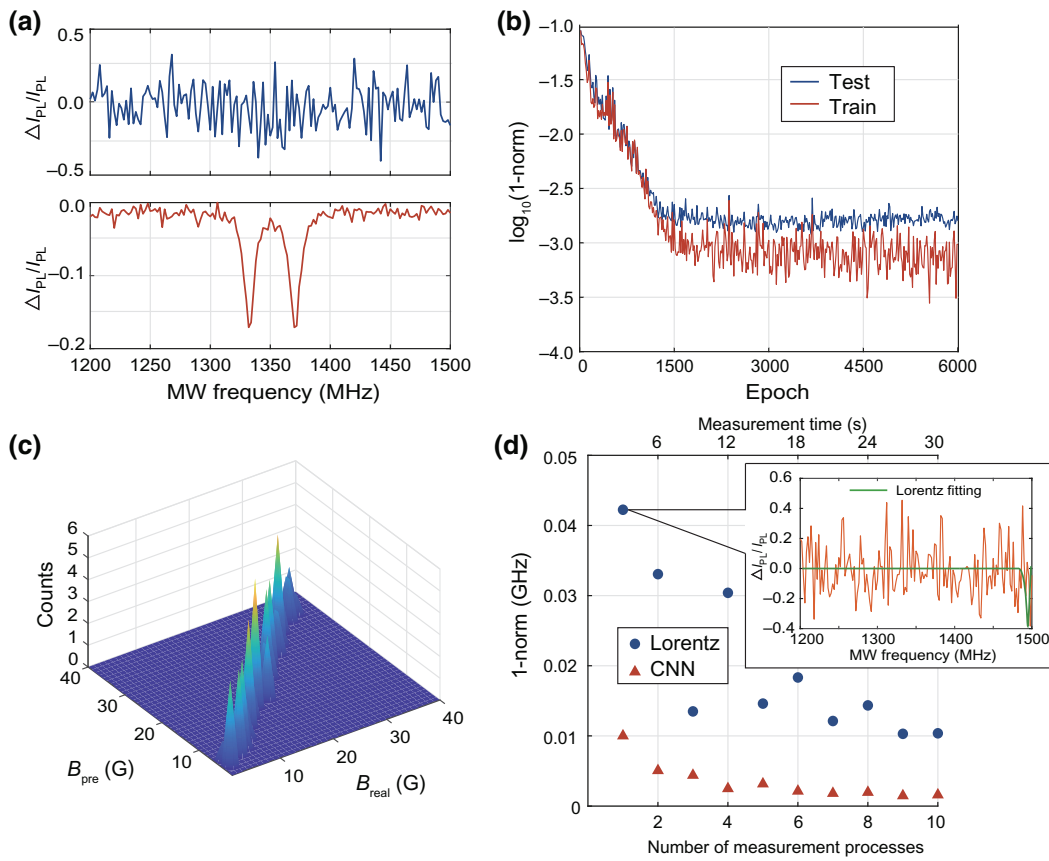


FIG. 3. Training data and results for ODMR signals. (a) ODMR signals with 1-time and 500-times measurement processes. (b) Performance of CNN with respect to epoch. (c) Matrix of prediction values  $B_{\text{pre}}$  and actual values  $B_{\text{real}}$ . (d) Comparison of different methods: 1-norm errors of positions predicted by Lorentz fitting and by the deep neural network. Some peaks in the ODMR data with few measurement times cannot be found by Lorentz fitting, as shown in the inset.

comparison between the Lorentz-fitting and deep-learning methods in the case of few measurements. When the number of measurement processes is less than 10, the 1-norm errors in the CNN-predicted peak positions are less than those calculated by Lorentz fitting. The errors decrease as the measurement time increases. The errors in the peak position fitted by Lorentz fitting undulate greatly, and the double peak cannot even be fitted at all using an individual one-time measurement process, as is shown in the inset of Fig. 3(d). This means that the Lorentz-fitting method is not efficient with few measurements. Besides, the time consumption for a prediction to obtain a certain precision, e.g.,  $10^{-2}$  GHz, with a well-trained CNN is much less than that for a Lorentz fitting, such that the CNN can predict the magnetic field strength in a timely way. Another way to scale the enhancement of the CNN method is to calculate the sensitivity of magnetic field sensing; the result also shows an improvement in the sensitivity with our method (see Appendix E for details).

To demonstrate the transferability of the CNN method described above in the context of ODMR learning, we apply it to predict the resonance frequencies of ODMR

spectra of another type of spin defect, i.e., a single PL1 defect. The spin-readout contrast and single-photon count rate of a single PL1 defect are both much lower than those of a single PL6 defect [25]. To obtain good performance of the CNN, the SNR of the input data should be similar to that of the training data. In the experiment, the SNR of the PL1 data accumulated in 500 measurement processes (the test data) is similar to that of the PL6 data accumulated in five measurement processes (the training data). The average 1-norm error of the prediction is about 4.2 MHz, which is comparable to that of the average error for the PL6 defect of 3.5 MHz (see Appendix D for more details).

Similarly, we investigate prediction of the Rabi-oscillation period with an extremely low SNR, assisted by the deep-learning method. Rabi oscillations obtained from one-time (upper panel) and 750-times (lower panel) measurement processes under the same conditions are shown in Fig. 4(a). For each point in an individual one-time measurement process, the pulse sequences, including optical initialization, microwave driving, and optical readout, are repeated 5400 times. Taking the results of the 750-times-repeated measurement processes as a standard, 6100 Rabi

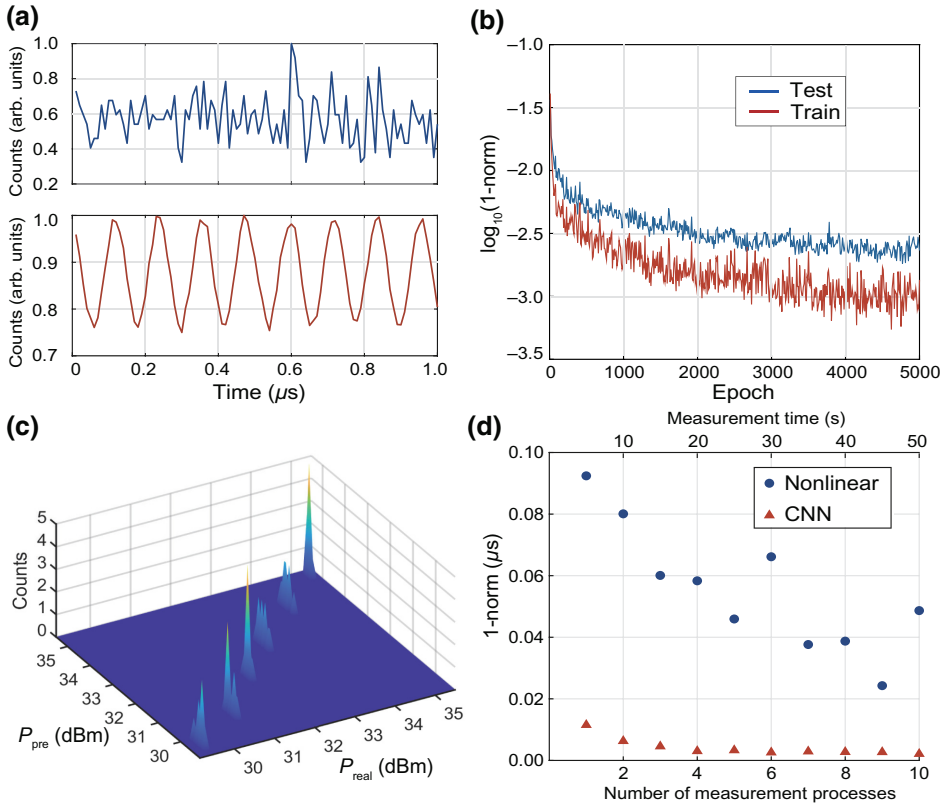


FIG. 4. Training data and results for Rabi oscillations. (a) Rabi-oscillation signal with 1-time and 750-times measurement processes. (b) Performance of the neural network with respect to epoch. (c) Matrix of predicted MW power  $P_{\text{pre}}$  and actual MW power  $P_{\text{real}}$  (dBm). (d) Comparison of different methods: 1-norm errors of oscillation periods predicted by nonlinear fitting and by the deep neural network.

oscillations (5500 training sets + 600 test sets) detected with 15 different MW powers (11 for the training sets, 4 for the test sets) with low SNR are labeled with their standard periods. The well-trained CNN can predict the period  $T$  when low-SNR Rabi oscillations are input. Unlike the CNN for the ODMR spectrum, the output layer that predicts the period has only one neuron. The training progress is shown in Fig. 4(b). The 1-norm errors of the training and test sets decrease as the epoch increases and reach about 1 ns when the epoch is greater than 5000. Moreover, the period  $T$  reflects the MW power  $P$ , and satisfies  $\sqrt{P} = C/T$ , where  $C$  is a coefficient of proportionality. Here we use 15 sets of MW-power–Rabi-oscillation-period data to fit the coefficient  $C$ , and obtain  $C = 5.07 \times 10^{-6} \text{ s mW}^{1/2}$ , with  $R^2 = 0.9997$ . The predicted MW power  $P_{\text{pre}}$  and the actual MW power  $P_{\text{real}}$  are shown in Fig. 4(c) and are distributed on the diagonal, which means that  $P_{\text{pre}} = P_{\text{real}}$ . Besides, the errors deduced for the deep-learning method are much less than those of the traditional fitting method for few measurements (when the number of measurement processes is less than ten), as shown in Fig. 4(d).

#### IV. CONCLUSIONS

In conclusion, we propose a deep-learning-enhanced method to detect the parameters of the ODMR spectra and Rabi oscillations of a single defect spin in SiC with one measurement process, which is more precise than the traditional fitting method. After training with a large number

of labeled samples, the CNN can predict the peak positions of the ODMR spectra or the frequency of the Rabi oscillations from a low-SNR signal with high speed and accuracy. In the prediction of the peak positions of the ODMR spectrum, the 1-norm errors can reach about 1 MHz, and the 1-norm errors are about 1 ns when the method is used to predict the period of Rabi oscillations. The accuracy might be further improved by dynamically changing the measurement time of the data in the training processes or using a decay learning rate.

The peaks in the ODMR spectrum and the Rabi-oscillation period are directly related to the magnetic and microwave field intensities, respectively [37]. A natural application is to sensing the noisy environment around a spin defect. The CNN can be trained in free time and then used for single-spin readout or real-time sensing of the corresponding parameters. In addition to the defect spins in SiC, this method can efficiently extract signals from other systems with strong noise.

#### ACKNOWLEDGMENTS

This work was supported by the National Key Research and Development Program of China (Grant No. 2016YFA0302700), the National Natural Science Foundation of China (Grants No. U19A2075, No. 61725504, No. 61905233, No. 11774335, No. 11821404, and No. 11975221), the Key Research Program of Frontier Sciences, CAS (Grant No. QYZDY-SSW-SLH003), the

Science Foundation of the CAS (Grant No. ZDRW-XH-2019-1), the Anhui Initiative in Quantum Information Technologies (Grants No. AHY060300 and No. AHY020100), the Fundamental Research Funds for the Central Universities (Grants No. WK2030380017 and No. WK2470000026), and the China Postdoctoral Science Foundation (Grants No. BX20200326 and 2021M693099). This work was partially carried out at the USTC Center for Micro and Nanoscale Research and Fabrication.

Y.-W. L., Q. L., and M. Y. contributed equally to this work.

## APPENDIX A: ARTIFICIAL NEURAL NETWORKS

Artificial neural networks (ANNs) are a computing model inspired by neural networks in biology, which can make predictions according to the input data after being trained [38]. A typical feedforward neural network consists of an input layer, hidden layers, and an output layer, as Fig. 5 shows.

The neurons in the hidden layers and output layer can be described by

$$\begin{aligned} a_i &= h(\theta_{i1}^{(1)} x_1 + \theta_{i2}^{(1)} x_2 + \theta_{i3}^{(1)} x_3), \\ b_i &= h(\theta_{i1}^{(2)} a_1 + \theta_{i2}^{(2)} a_2 + \theta_{i3}^{(2)} a_3 + \theta_{i4}^{(2)} a_4), \\ y &= h(\theta_1^{(3)} b_1 + \theta_2^{(3)} b_2 + \theta_3^{(3)} b_3 + \theta_4^{(3)} b_4), \end{aligned} \quad (\text{A1})$$

where  $x_i$  is the input data,  $y$  is the output data, and  $a_i$  and  $b_i$  are the hidden neurons. The matrix  $\Theta$  determines the mapping from the  $i$ th layer to the  $(i + 1)$ th layer.  $h(z)$  is the activation function, which can include nonlinear relations such as tanh, ReLu, and sigmoid functions in the network.

The loss function is another concept that plays an important role in machine learning. This is a kind of function

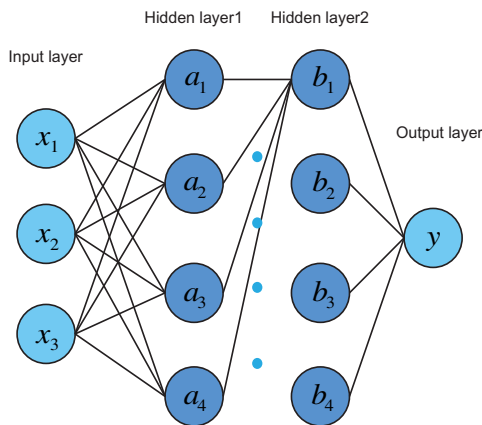


FIG. 5. Basic architecture of an ANN. Each circle stands for a neuron, and the lines show the connections between different neurons. The ANN has four layers: an input layer, two hidden layers, and an output layer.

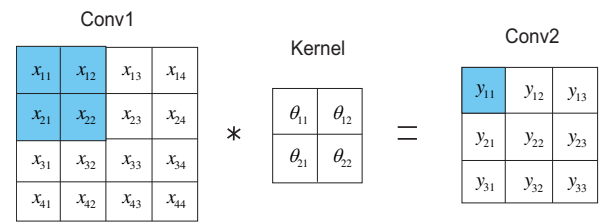


FIG. 6. Convolution. The input matrix  $X$  is mapped to the output matrix  $Y$  by convolution. The blue block in  $Y$  is calculated by summing the blue region in  $X$  with the weights in the kernel  $\Theta$ .

used for evaluating the predictions of networks by calculating the differences between the real values and the predicted values. For example, we use a loss function called the cross-entropy when using ANNs for classification. In a binary classification task, this function can be expressed as

$$\begin{aligned} L(\theta) &= \frac{1}{N} \sum_k L_k \\ &= \frac{1}{N} \sum_k -[p_k \ln(y_k) + (1 - p_k) \ln(1 - y_k)], \end{aligned} \quad (\text{A2})$$

where  $N$  is the total number of training data,  $p_k$  is the label of the training data (true,  $p_k = 1$ ; false,  $p_k = 0$ ), and  $y_k$  is the probability that the  $k$ th sample given by the ANN is true. It is obvious that with a decreasing value of  $L$ , the accuracy of the prediction of the ANN rises. So, the training process of the ANN minimizes  $L$  using the backpropagation method [39]. When the network has been trained on each training sample once, we say that one epoch has finished. The training process usually consists of more than one epoch.

The CNN that we use here is that of a deep-learning method in which data flow from one layer to another by convolution, as shown in Fig. 6. The matrix  $X$  is the input data (an image in most cases), the matrix  $\Theta$  is the convolution index, called the convolution kernel, and the matrix  $Y$  is the output data after convolution. It is calculated as

$$y_{11} = \theta_{11}x_{11} + \theta_{12}x_{12} + \theta_{21}x_{21} + \theta_{22}x_{22}. \quad (\text{A3})$$

By moving the blue region in the matrix  $X$  from left to right and from top to bottom, we can get the output matrix  $Y$ .

## APPENDIX B: DETAILS OF THE CNN

The structure of the neural network (see Fig. 1) that we propose for learning from ODMR and Rabi images is based on the basic convolutional neural network. The CNN consists of three convolution units, each of which includes a convolutional layer with filter size  $1 \times 1$ , a ReLu activation function, and a max-pooling layer with  $1 \times 2$  strides.

Following the three units are two fully connected layers and a linear output layer. We train our network using the TensorFlow framework, and the training process is accelerated by two NVIDIA 1080Ti graphics processing units.

## APPENDIX C: DETAILS OF ODMR AND RABI EXPERIMENTS

### 1. Sample preparation

In the present work, an epitaxial layer of single-crystal  $4H$ -SiC with a nitrogen concentration of  $5 \times 10^{15} \text{ cm}^{-3}$  is used. Through electron-beam lithography, ion implantation, and annealing techniques, an array of single divacancy defects with a pitch of about  $2 \mu\text{m}$  is fabricated in a shallow layer beneath the surface of the  $4H$ -SiC sample. The sample is then cleaned in a 3:1 mixture of concentrated sulfuric acid and hydrogen peroxide heated to  $95^\circ\text{C}$  for 5 h, which dramatically reduces the background fluorescence so that single defect spin qubits can be optically addressed and individually manipulated [25,40].

### 2. Fluorescence imaging and ODMR measurements

A room-temperature home-built scanning confocal microscope combined with an ODMR measurement system is used to individually address and coherently control single spin qubits in the SiC. The experimental setup is shown in Fig. 7. A 914-nm CW laser, modulated by an acousto-optic modulator and focused by an infrared oil objective (Nikon, NA = 1.3), is used to excite single divacancy spin qubits. A long-pass dichroic mirror (Semrock) is used to separate the laser and fluorescence signals. The SiC sample is mounted on a closed-cycle three-axis piezoelectric stage. The fluorescence signals, filtered by a long-pass filter, are coupled to a single-mode fiber and then detected by a superconducting-nanowire single-photon detector (Scontel). The photon counts are recorded by a counter (not shown in the experimental setup).

For the ODMR and Rabi measurements, microwave sequences are generated by a microwave generator (Mini-Circuits, SSG-6000 RC) and then gated by a switch (Mini-Circuits, ZASWA-2-50DR+). After being amplified by an amplifier (Mini-Circuits, ZHL-25W-272+), the microwave signals are fed to a  $50\text{-}\mu\text{m}$ -wide copper wire above the surface of the sample. The timing sequence of the electrical signals for manipulating and synchronizing the laser, microwave generator, and counter is generated by a pulse generator (SpinCore). A static magnetic field parallel to the  $c$  axis of the  $4H$ -SiC is manipulated by an electromagnet. A modulated laser pulse is used to polarize and read out the optical signals, depending on the spin states of the isolated defects [25,35,36].

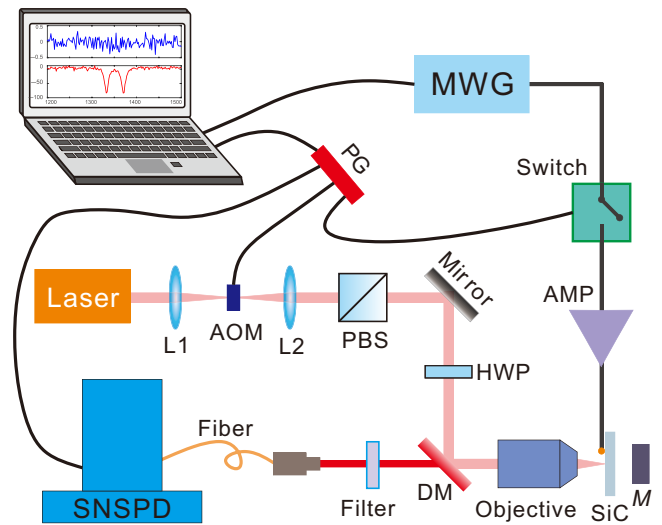


FIG. 7. Experimental setup. A home-built scanning confocal microscope system is used in our experiments. A 914-nm CW laser is modulated by an acousto-optic modulator (AOM), after which the laser beam is reflected by a long-pass dichroic mirror (DM) and then focused by an objective in order to excite single point-defect spin qubits in  $4H$ -SiC. The polarization of the laser is adjusted by a polarizing beamsplitter (PBS) and a half-wave plate (HWP). The photoluminescence is collected by the same objective and filtered by a long-pass filter, and is ultimately detected by a superconductive-nanowire single-photon detector (SNSPD). The number of photons is recorded by a counter. Microwave sequences are generated by a microwave generator (MWG) and then gated by a switch. After being amplified by an amplifier (AMP), the microwave signals are fed to a  $50\text{-}\mu\text{m}$ -wide copper wire above the surface of the  $4H$ -SiC sample. The timing sequence of the electrical signals for manipulating and synchronizing the laser, microwave generator, and counter is generated by a pulse generator (PG). A static magnetic field parallel to the  $c$  axis of the  $4H$ -SiC is manipulated by an electromagnet (M).

### 3. Pulse sequences for the ODMR and Rabi-oscillation measurements

Because of the spin-polarization-dependent emission,  $\Delta I_{\text{PL}}$  with and without resonant MWs can be detected, which is the basis of the CW ODMR measurements. ODMR spectra are measured by scanning the microwave frequency from 1200 to 1500 MHz with a step size of 2 MHz. For each point in a single one-time measurement process, the MW signal is gated on and off with a 1-ms duration and repeated ten times, such that the one-time measurement process of the ODMR spectrum consumes 3 s. The pulse sequence for an individual one-time ODMR measurement process is shown in Fig. 8(a), in which the red and blue squares represent the laser and MW pulse sequences, respectively. Figure 8(b) shows the pulse sequence for an individual Rabi-oscillation measurement process. The first  $3\text{-}\mu\text{s}$  laser pulse is used to initialize the single spin qubit to the state  $m_s = 0$ , and the laser is

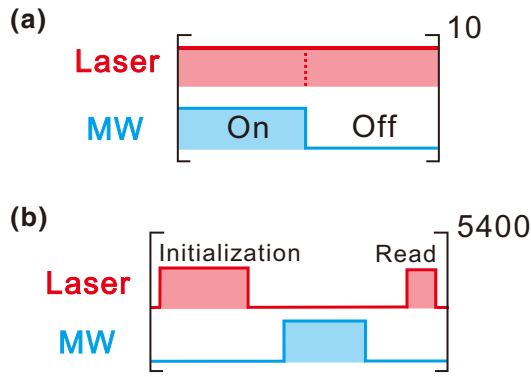


FIG. 8. Pulse sequences. (a) An individual one-time ODMR measurement process. (b) An individual one-time Rabi-oscillation measurement process.

then turned off for  $1 \mu\text{s}$ , such that the state goes back to the spin ground state. A microwave pulse of varying length is applied to drive the spin qubit such that the spin state oscillates between the states  $m_s = 0$  and  $m_s = -1$ ; the MW duration is changed from 20 ns to  $1.02 \mu\text{s}$  with 100 equally spaced sampling points. Finally, a laser read pulse (the duration time of which is set to  $0.3 \mu\text{s}$ ) is used to read out the state's population through the photon counts. For each one-time Rabi-oscillation measurement process, the pulse sequences are repeated 5400 times, such that the time consumption is about 5 s.

#### APPENDIX D: TRANSFERABILITY OF THE CNN

We use the CNN trained with the data from the first PL6 defect to predict the ODMR resonance frequencies of another PL6 defect at five magnetic field intensities (different from those for the first PL6 defect). The predicted 1-norm errors are shown in Fig. 9(a). The blue triangles represent the average 1-norm errors, which decrease with an increase in the number of measurement processes. The tendency and the errors are similar to those shown in Fig. 3(d). Therefore, the CNN has learned the general features of the PL6 defect's ODMR signal from the training data.

We then extend the application of the CNN method to predict the ODMR properties of a different kind of defect, i.e., a single PL1 defect, which has a much lower spin-readout contrast and single-photon count rate than those of the PL6 defect [25]. To have good performance of the CNN, it is better for the test data and the training data to have similar SNRs. In the experiment, the CNN is trained with PL6 data accumulated in five measurement processes, and the input data are PL1 data accumulated in 500 measurement processes, since these data have a similar SNR. The ODMR resonance frequencies are measured at five different magnetic fields. The predicted 1-norm error at each magnetic field is shown in Fig. 9(b). The average error

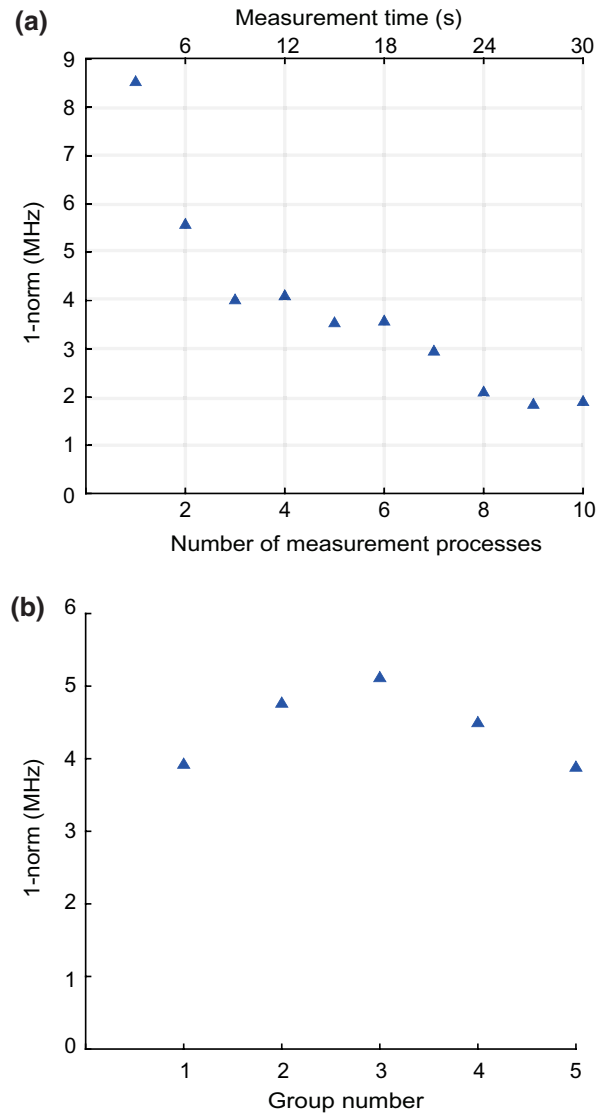


FIG. 9. Experimental results for the second PL6 defect and the PL1 defect. (a) 1-norm errors of the predicted ODMR resonance frequencies for different measurement processes. (b) 1-norm errors of the predicted ODMR spectra of a single PL1 defect obtained with the CNN trained with the PL6 data.

is calculated to be about 4.2 MHz, which is comparable to the result for the PL6 defect of about 3.5 MHz. As a result, the CNN trained with the data for the PL6 defect not only can be applied to predict the ODMR properties of other PL6s but also can predict the properties other kinds of defects in SiC. The transferability of the CNN could be of potential broad application.

#### APPENDIX E: SENSITIVITY OF MAGNETIC FIELD SENSING

The sensitivity is calculated as

$$\eta^2 = \delta B^2 = \sigma^2(B)T, \quad (\text{E1})$$



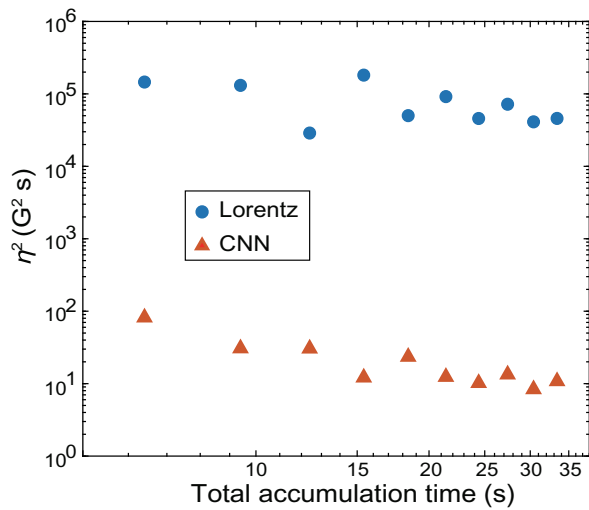


FIG. 10. Sensitivity of magnetic field sensing for different methods.

where  $\sigma^2(B)$  is the scaling of the prediction errors and  $T$  is the total accumulation time for the measurement. Here we use the square of the 1-norm error as the prediction error for magnetic field sensing, and we omit the time consumption for data communication in the estimation. So, the total accumulation time is  $T_{\text{total}} = T_m + T_{\text{CNN}}$ , where  $T_m$  is the time spent on measurement processes, and  $T_{\text{CNN}}$  is the time consumption of the CNN algorithm (about 3.4 s). The sensitivity of magnetic field sensing with and without the CNN is shown in Fig. 10. The triangles show a slow decline of the sensitivity as  $T$  increases, which means that the precision increases with a longer measurement time. We obtain a square of the sensitivity of  $1.1 \times 10^1 \text{ G}^2 \text{ s}$  when the total accumulation time reaches 33.4 s. The figure also supports our conclusion in the main text, since the sensitivity is significantly improved by the deep-learning-enhanced method.

[1] W. F. Koehl, B. B. Buckley, F. J. Heremans, G. Calusine, and D. D. Awschalom, Room temperature coherent control of defect spin qubits in silicon carbide, *Nature* **479**, 84 (2011).  
 [2] M. Atatüre, D. Englund, N. Vamivakas, S.-Y. Lee, and J. Wrachtrup, Material platforms for spin-based photonic quantum technologies, *Nat. Rev. Mater.* **3**, 38 (2018).  
 [3] D. D. Awschalom, R. Hanson, J. Wrachtrup, and B. B. Zhou, Quantum technologies with optically interfaced solid-state spins, *Nat. Photon.* **12**, 516 (2018).  
 [4] S. Castelletto and A. Boretti, Silicon carbide color centers for quantum applications, *J. Phys.: Photon.* **2**, 022001 (2020).  
 [5] N. T. Son, C. P. Anderson, A. Bourassa, K. C. Miao, C. Babin, M. Widmann, M. Niethammer, J. Ul Hassan, N.

Morioka, I. G. Ivanov, F. Kaiser, J. Wrachtrup, and D. D. Awschalom, Developing silicon carbide for quantum spintronics, *Appl. Phys. Lett.* **116**, 190501 (2020).  
 [6] G. Zhang, Y. Cheng, J.-P. Chou, and A. Gali, Material platforms for defect qubits and single-photon emitters, *Appl. Phys. Lett.* **7**, 031308 (2020).  
 [7] V. A. Norman, S. Majety, Z. Wang, W. H. Casey, N. Curro, and M. Radulaski, *Novel color center platforms enabling fundamental scientific discovery*. *InfoMat.*, 1, (2020).  
 [8] D. J. Christle, A. L. Falk, P. Andrich, P. V. Klimov, J. U. Hassan, N. T. Son, E. Janzen, T. Ohshima, and D. D. Awschalom, Isolated electron spins in silicon carbide with millisecond coherence times, *Nat. Mater.* **14**, 160 (2015).  
 [9] M. Widmann, S.-Y. Lee, T. Rendler, N. T. Son, H. Fedder, S. Paik, L.-P. Yang, N. Zhao, S. Yang, I. Booker, A. Denisenko, M. Jamali, S. A. Momenzadeh, I. Gerhardt, T. Ohshima, A. Gali, E. Janzén, and J. Wrachtrup, Coherent control of single spins in silicon carbide at room temperature, *Nat. Mater.* **14**, 164 (2015).  
 [10] F. Fuchs, B. Stender, M. Trupke, D. Simin, J. Pflaum, V. Dyakonov, and G. V. Astakhov, Engineering near-infrared single-photon emitters with optically active spins in ultrapure silicon carbide, *Nat. Commun.* **6**, 7578 (2015).  
 [11] J.-F. Wang, F.-F. Yan, Q. Li, Z.-H. Liu, H. Liu, G.-P. Guo, L.-P. Guo, X. Zhou, J.-M. Cui, J. Wang, Z.-Q. Zhou, X.-Y. Xu, J.-S. Xu, C.-F. Li, and G.-C. Guo, Coherent Control of Nitrogen-Vacancy Center Spins in Silicon Carbide at Room Temperature, *Phys. Rev. Lett.* **124**, 223601 (2020).  
 [12] V. Ivády, J. Davidsson, N. Deegan, A. L. Falk, P. V. Klimov, S. J. Whiteley, S. O. Hruszkewycz, M. V. Holt, F. J. Heremans, N. T. Son, D. D. Awschalom, I. A. Abrikosov, and A. Gali, Stabilization of point-defect spin qubits by quantum wells, *Nat. Commun.* **10**, 5607 (2019).  
 [13] S. Castelletto, Silicon carbide single-photon sources: Challenges and prospects, *Mater. Quantum Technol.* **1**, 023001 (2021).  
 [14] C. P. Anderson, A. Bourassa, K. C. Miao, G. Wolfowicz, P. J. Mintun, A. L. Crook, H. Abe, J. U. Hassan, N. T. Son, T. Ohshima, and D. D. Awschalom, Electrical and optical control of single spins integrated in scalable semiconductor devices, *Science* **366**, 1225 (2019).  
 [15] M. Widmann, M. Niethammer, D. Y. Fedyanin, I. A. Khramtsov, T. Rendler, I. D. Booker, J. U. Hassan, N. Morioka, Y.-C. Chen, I. G. Ivanov, N. T. Son, T. Ohshima, M. Bockstedte, A. Gali, C. Bonato, S.-Y. Lee, and J. Wrachtrup, Electrical charge state manipulation of single silicon vacancies in a silicon carbide quantum optoelectronic device, *Nano. Lett.* **19**, 7173 (2019).  
 [16] N. T. Son, E. Sörman, W. M. Chen, C. Hallin, and J. L. Lindström, Optically detected magnetic resonance studies of defects in electron-irradiated 3C SiC layers, *Phys. Rev. B* **55**, 2863 (1997).  
 [17] M. Brune, F. Schmidt-Kaler, A. Maali, J. Dreyer, E. Hagley, J. M. Raimond, and S. Haroche, Quantum Rabi Oscillation: A Direct Test of Field Quantization in a Cavity, *Phys. Rev. Lett.* **76**, 1800 (1996).  
 [18] G.-Y. Liu, M. Chen, Y.-X. Liu, D. Layden, and P. Cappellaro, Repetitive readout enhanced by machine learning, *Mach. Learn. Sci. Technol.* **1**, 015003 (2020).

- [19] Z. A. Kudyshev, S. I. Bogdanov, T. Isacson, A. V. Kildishev, A. Boltasseva, and V. M. Shalaev, Rapid classification of quantum sources enabled by machine learning, *Adv. Quantum Technol.* **3**, 2000067 (2020).
- [20] N. Aharon, A. Rotem, L. P. McGuinness, F. Jelezko, A. Retzker, and Z. Ringel, NV center based nano-NMR enhanced by deep learning, *Sci. Rep.* **9**, 17802 (2019).
- [21] R. Santagati, A. A. Gentile, S. Knauer, S. Schmitt, S. Paesani, C. Granade, N. Wiebe, C. Osterkamp, L. P. McGuinness, J. Wang, M. G. Thompson, J. G. Rarity, F. Jelezko, and A. Laing, Magnetic-Field Learning Using a Single Electronic Spin in Diamond with One-Photon Readout at Room Temperature, *Phys. Rev. X* **9**, 021019 (2019).
- [22] K. Fukushima, Neocognitron: A self-organizing neural network model for a mechanism of pattern recognition unaffected by shift in position, *Biol. Cybern.* **36**, 193 (1980).
- [23] K. Jarrett, K. Kavukcuoglu, M. Ranzato, and Y. Lecun, *What is the best multi-stage architecture for object recognition?* Proc International Conference on Computer Vision. IEEE, (2009).
- [24] D. P Kingma and J. Ba, *Adam: A Method for Stochastic Optimization*. CoRR **abs/1412.6980** (2014).
- [25] Q. Li, J.-F. Wang, F.-F. Yan, J.-Y. Zhou, H.-F. Wang, H. Liu, L.-P. Guo, X. Zhou, A. Gali, Z.-H. Liu, Z.-Q. Wang, K. Sun, G.-P. Guo, J.-S. Tang, H. Li, L. X. You, J.-S. Xu, C.-F. Li, and G.-C. Guo, *Room temperature coherent manipulation of single-spin qubits in silicon carbide with a high readout contrast*. Natl. Sci. Rev. (2021),.
- [26] J.-Y. Zhou, Q. Li, Z.-Y. Hao, F.-F. Yan, M. Yang, J.-F. Wang, W.-X. Lin, Z.-H. Liu, W. Liu, H. Li, L. You, J.-S. Xu, C.-F. Li, G.-C. Guo, Experimental determination of the dipole orientation of single color centers in silicon carbide, *ACS Photonics* **8**, 2384 (2021).
- [27] A. Gruber, A. Drabenstedt, C. Tietz, L. Fleury, J. Wrachtrup, and C. von Borczyskowski, Scanning confocal optical microscopy and magnetic resonance on single defect centers, *Science* **276**, 2012 (1997).
- [28] A. Dréau, M. Lesik, L. Rondin, P. Spinicelli, O. Arcizet, J. F. Roch, and V. Jacques, Avoiding power broadening in optically detected magnetic resonance of single NV defects for enhanced dc magnetic field sensitivity, *Phys. Rev. B* **84**, 195204 (2011).
- [29] B. Lounis and M. Orrit, Single-photon sources, *Rep. Prog. Phys.* **68**, 1129 (2005).
- [30] S. Castelletto, B. C. Johnson, V. Ivády, N. Stavrias, T. Umeda, A. Gali, and T. Ohshima, A silicon carbide room-temperature single-photon source, *Nat. Mater.* **13**, 151 (2014).
- [31] J. Wang, Y. Zhou, Z. Wang, A. Rasmita, J. Yang, X. Li, H. J. von Bardeleben, and W. Gao, Bright room temperature single photon source at telecom range in cubic silicon carbide, *Nat. Commun.* **9**, 4106 (2018).
- [32] Y. Zhou, Z. Wang, A. Rasmita, S. Kim, A. Berhane, Z. Bodrog, G. Adamo, A. Gali, I. Aharonovich, and W. Gao, Room temperature solid-state quantum emitters in the telecom range, *Sci. Adv.* **4**, eaar3580 (2018).
- [33] A. L. Falk, B. B. Buckley, G. Calusine, W. F. Koehl, V. V. Dobrovitski, A. Politi, C. A. Zorman, P. X.-L. Feng, and D. D. Awschalom, Polytype control of spin qubits in silicon carbide, *Nat. Commun.* **4**, 1819 (2013).
- [34] J.-F. Wang, J.-M. Cui, F.-F. Yan, Q. Li, Z.-D. Cheng, Z.-H. Liu, Z.-H. Lin, J.-S. Xu, C.-F. Li, and G.-C. Guo, Optimization of power broadening in optically detected magnetic resonance of defect spins in silicon carbide, *Phys. Rev. B* **101**, 064102 (2020).
- [35] J. F. Wang, Y. Zhou, X. M. Zhang, F. C. Liu, Y. Li, K. Li, Z. Liu, G. Z. Wang, and W. B. Gao, Efficient Generation of an Array of Single Silicon-Vacancy Defects in Silicon Carbide, *Phys. Rev. Appl.* **7**, 064021 (2017).
- [36] F.-F. Yan, J.-F. Wang, Q. Li, Z.-D. Cheng, J.-M. Cui, W.-Z. Liu, J.-S. Xu, C.-F. Li, and G.-C. Guo, Coherent Control of Defect Spins in Silicon Carbide above 550 K, *Phys. Rev. Appl.* **10**, 044042 (2018).
- [37] L. Rondin, J.-P. Tetienne, T. Hingant, J.-F. Roch, P. Maletinsky, and V. Jacques, Magnetometry with nitrogen-vacancy defects in diamond, *Rep. Prog. Phys.* **77**, 056503 (2014).
- [38] J. Hertz, A. Krogh, R. Palmer, and R. V. Jensen, Introduction to the theory of neural computation, *Am. J. Phys.* **62**, 668 (1994).
- [39] D. E. Rumelhart, G. E. Hinton, and R. J. Williams, Learning representations by back propagating errors, *Nature* **323**, 533 (1986).
- [40] J.-F. Wang, Q. Li, F.-F. Yan, H. Liu, G.-P. Guo, W.-P. Zhang, X. Zhou, L.-P. Guo, Z.-H. Lin, J.-M. Cui, X.-Y. Xu, J.-S. Xu, C.-F. Li, and G.-C. Guo, On-demand generation of single silicon vacancy defects in silicon carbide, *ACS Photonics* **6**, 1736 (2019).